

## Study on Axial Stretching Mechanical Property of Plant Fiber-reinforced Cementitious Composites

Xinyuan Wang<sup>1)</sup>, Zongfeng He<sup>2)</sup>, Xiaocheng Ma<sup>2)</sup>, Qing Cui<sup>2)</sup> and Xuansheng Cheng<sup>1)\*</sup>

<sup>1)</sup>Lanzhou University of Technology, China.

\* Corresponding Author. E-Mail: chengxslut@sina.com

<sup>2)</sup>Gansu First Construction Group Co., Ltd, China.

### ABSTRACT

This paper aims to explore the tensile properties of plant fiber-reinforced cementitious composites (PFRCCs). An axial tensile numerical-simulation and test study of PFRCC panels with four thicknesses was performed to analyze their tensile properties, providing a relevant basis for the engineering application of PFRCC panels. The results show that the peak load of uniaxial tensile failure of PFRCC panels with thicknesses of 8 mm, 12 mm, 15 mm and 18 mm is 424.0 N, 664.8 N, 825.0 N and 986.4 N, respectively. The bearing capacity of the panels gradually increases with the increase of the thickness. The peak tensile strain is about 0.044%, 2.93 times that of the cement matrix and the tensile strength is about 2.73 MPa. It is proved that adding plant fiber can increase the toughness of the cement matrix and increasing PFRCC panel thickness can improve its tensile bearing capacity without affecting its tensile-strength.

**KEYWORDS:** Composite materials, Cement matrix, Plant fiber, Axial tension.

### INTRODUCTION

With the development of urban construction, building energy consumption is increasing year by year. Building energy consumption will dominate energy consumption for a long time. Therefore, it is urgent to improve the energy efficiency of buildings. The plant fiber-reinforced cementitious composites (PFRCCs) have the advantages of environmental protection, energy saving, lightweight and high strength. Therefore, to better apply PFRCC panels to practical projects, such as the permanent formwork of foundation beam and light-gauge steel stud-concrete composite external wall panels, this paper uses a combination of numerical simulation and tests to analyze its tensile properties in detail.

The widely used fibers include asbestos fiber, carbon fiber, polyethylene fiber, polypropylene fiber, steel fiber, fine polypropylene fiber, polyvinyl alcohol (PVA)

fiber, plant fiber, ...etc. In view of the above fiber materials, scholars have carried out a large number of research studies on mechanical properties. Li (1998) applied the basic principles of fracture mechanics and micromechanics to cementitious composites for the first time to analyze the interaction of fiber and cement matrix and summarized the design concept of fiber-reinforced cement-based composites. Bahja et al. (2021) found that adding 4% sisal fiber to cement would reduce its density and increase its porosity. Mathews et al. (2021) studied the bond strength of self-compacting concrete made of fly ash, ground granulated blast-furnace slag and expanded perlite aggregate under elevated-temperature exposure. Zukowski et al. (2018) described the design process of natural fiber-reinforced strain-hardened cementitious composites. Matrix-fracture energy and matrix-fiber bond were investigated and implemented into a theoretical model of critical fiber-volume prediction, which was verified by mechanical tests of tensile, bending and compression strengths. Santos et al. (2021) introduced the properties of nanocellulose, their generation and the effect of

---

Received on 17/3/2023.

Accepted for Publication on 24/10/2023.

nanocellulose on cementitious composites, observing that the incorporation of nanocellulose brought about the relevant improvement in mechanical properties. Ferreira et al. (2017) investigated the effects of hornification on the chemical and mechanical behaviors of natural fibers and how these properties affect the fiber-matrix bond. Li et al. (2018) conducted steam explosion and bleaching pretreatment of straw fibers. The effects of the composition and structure of plant fibers on the hydration and mechanical properties of cementitious composites were studied. Alrekabi et al. (2017) showed that hybrid fiber composites with synergistic effects of nano- and micro-additives could potentially lead to significant improvements in the toughness and mechanical properties of fiber-reinforced cementing materials. Wang et al. (2017) showed that sisal fiber can increase the compressive strength of concrete to some extent, which can be improved by about 9% compared with ordinary concrete when the optimal dosage is  $2\text{kg/m}^3$ . Bi et al. (2021) established a new constitutive model of steel fiber-reinforced concrete by considering the bonding effect between fiber and concrete and simulated the tensile and four-point bending tests of steel fiber-reinforced concrete, which was found to fit well with the test data. Shang et al. (2019) obtained the tensile properties of four plant fiber-reinforced cementitious materials, such as bamboo raw, hemp, sisal and ramie fibers, by uniaxial tensile tests and the study showed that the fiber concrete had good retention of stress levels. Yao et al. (2022) obtained the uniaxial tensile properties of sea-sand ECC materials by a uniaxial tensile test with the content of PE fiber and PVA fiber as variables. Liu and Zhang (2019) showed that the toughening effect of fiber-reinforced cementitious composites is caused by interfacial shear stress rather than fiber tensile stress and that the higher the fiber modulus, the higher the load-bearing capacity, but not the higher the composite toughness. Kavya et al. (2022) constructed a deep-learning algorithm for predicting the bending, splitting tensile and compressive strengths of steel fiber-reinforced concrete.

In summary, many scholars have tried to change the mechanical properties of cementitious materials by adding different kinds of fiber to the cement matrix, but few studies have dealt with the effect of changing the thickness of fiber-reinforced cementitious composites on uniaxial tensile mechanical properties. In this paper,

a detailed study of the tensile properties of several commonly used thicknesses of PFRCC panels is carried out by axial tensile tests. It provides a more theoretical basis for the engineering application of PFRCC panels.

### CONSTRUCTION OF A THREE-DIMENSIONAL RANDOM DISTRIBUTION MODEL OF FIBERS

The distribution of a large number of fibers in the cement matrix presents a random and disordered distribution. To truly simulate the random distribution of fibers in the PFRCC panels and establish a more realistic finite-element model, it is necessary to study the algorithm of random distribution of fibers in the cement matrix. In this paper, the Monte Carlo method is used. The fiber random-distribution model is constructed through the secondary development of finite-element simulation software. The steps of fiber generation are shown in Fig. 1.

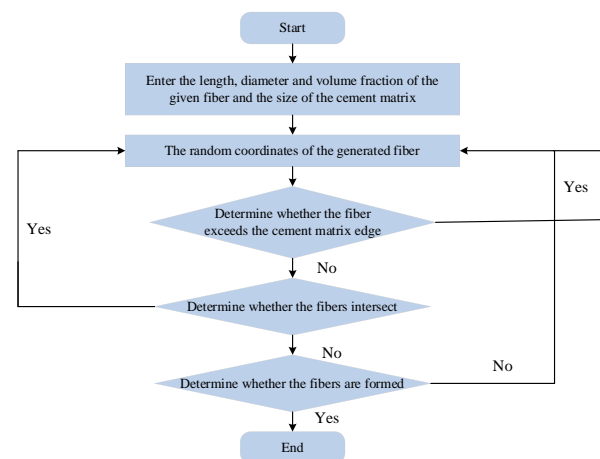


**Figure (1): Flowchart of fiber random-placement algorithm**

### FIBER-MATRIX JOINT CONSTITUTIVE RELATION MODEL

#### *Selection of Constitutive Relation between Fiber and Matrix*

At present, there are few types of research on the constitutive relation of cement mortar in ABAQUS. A mature approach is to treat mortar as concrete without coarse aggregate and use the constitutive-relation model of concrete to replace the constitutive relation of mortar.

Combined with the actual situation, the plastic-damage model is selected as the constitutive curve of mortar. The performance parameters of M45 mortar are as follows: the cracking strength is 2.2MPa, the elastic modulus is 25GPa, Poisson's ratio is 0.2 and the density is 2.0kg/cm<sup>3</sup>. (Chai, 2019).

The plant fiber is selected from bamboo fiber and the surface of this fiber is specially treated to achieve strain hardening effect effectively. The main performance parameters of the fiber are shown in Table 1 and the principal structure relationship curve is shown in Fig. 2.

**Table 1. Main performance parameters of bamboo fiber**

Density (g/cm <sup>3</sup> )	Tensile strength/MPa	Diameter/μm	Elastic modulus/GPa	Extension at Break/%	Length/mm
1.1	350	17	22	5.8	2.04

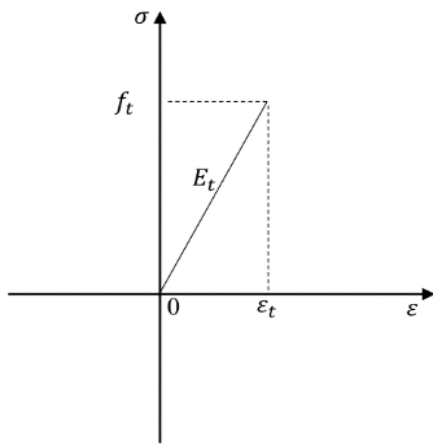


**Figure (2): Fiber constitutive-relation curve**

**Numerical Simulation of Single-fiber Pull-out**

An important method to study cement-based fiber-composite materials is the load-displacement relationship curve of a single-fiber pull-out from a cement matrix. The curve can reflect the performance change of the fiber in the cement matrix, so as to measure the relevant performance parameters of the fiber interface. Therefore, this paper referred to the single-fiber pull-out test of plant fiber in a cement matrix by Kochova et al. (2020) combined with finite-element numerical simulation and proposed fiber-matrix joint constitutive-relation model.

The main functions of plant fiber in cement matrix can be divided into three stages: interfacial elastic stage, debond stage and slip stage. In the fiber monofilament pull-out theory of Li (1993), the interface elastic stage is neglected and it is considered that when the fiber slips in the cement matrix, the elastic elongation of the fiber

itself can be neglected compared with the slip displacement generated by the fiber. Therefore, the fiber can be considered as a rigid body, ignoring the influence of the elastic elongation of the fiber itself and only considering the rigid body displacement of the fiber in the cement matrix. In addition, the debond and slip processes of fiber pulling-out in cement matrix are studied systematically and the relationship between the external load and pulling-out the displacement of fiber at different stages is proposed. He concluded that the unbonded part of the fiber during debonding is mainly controlled by the chemical-bonding force, which is mainly controlled by a parameter  $G_d$  that represents the chemical-bonding properties between the fiber and the matrix. The elastic elongation of the debonded fiber occurs in the cement matrix and the sliding-friction force remains unchanged at the initial sliding-friction force of  $\tau_0$  and it is evenly distributed along the debonded fiber. The slippage stage of fiber is mainly controlled by the sliding-friction force. Li proposed to use the friction factor  $\beta$  to describe the variation of the sliding-friction force of fiber. In addition, Li believed that the bending and surface roughness of fiber in a cement matrix would reduce the Poisson's ratio effect, so the influence of fiber Poisson's ratio was not considered. Li gives the displacement relationship between the external load  $P$  of the fiber at the pull-out end and the displacement of the fiber relative to the matrix cracking surface  $\delta$ , as shown in Eq. (1):

$$P = \sqrt{\frac{\pi^2 \tau_0 E_f d_f^3 (1 + \eta)}{2} \delta + \frac{\pi^2 G_d E_f d_f^3}{2}} \quad (0 \leq \delta \leq \delta_0) \quad (1)$$

where  $\tau_0$  is the initial sliding-friction force,  $E_f$  is the fiber elastic modulus,  $d_f$  is the fiber diameter,  $\eta$  is a parameter representing the ratio of effective fiber stiffness to effective matrix stiffness,  $G_d$  is the chemical-debonding energy,  $\delta$  is the displacement of the fiber relative to the matrix cracking surface,  $\delta_0$  is the maximum pull-out displacement of the fiber in the debonding stage, which can be obtained from Eq. (2).  $L_e$  is the embedding depth of plant fiber.

$$\delta_0 = \frac{2\tau_0 L_e^2 (1 + \eta)}{E_f d_f} + \sqrt{\frac{8G_d L_e^2 (1 + \eta)}{E_f d_f}} \quad (2)$$

The fiber in the glide phase is mainly controlled by sliding friction, Li proposed a friction factor  $\beta$  to distinguish the variation of the sliding-friction force of different fibers.  $\beta < 0$ , slippage softening;  $\beta = 0$ , constant friction slip;  $\beta > 0$ , slip hardening. Aiming at the slip-hardening phenomenon, Li proposed a linear-change model of the interfacial shear stress behind the slip-hardening phenomenon, as shown in Eq. (3):

$$\tau = \tau_0 \left( 1 + \beta \frac{S}{d_f} \right) \quad (3)$$

where  $S = \delta - \delta_0$ , considering that the fiber is a rigid body in the slip stage and there is only a uniform sliding-friction force  $\tau$  on the fiber surface. For the fiber with buried length  $L_e$ , the relationship between drawing load  $P$  and fiber drawing displacement  $\delta$  can be obtained, as shown in Eq. 4. Table 2 lists the parameters on the interface (Li, 1993; Guo et al., 2022):

$$p = \pi d_f \tau_0 (1 + \beta(\delta - \delta_0)) / d_f (L_e - \delta + \delta_0), \quad (4)$$

**Table 2. The main performance parameters of the interface**

Parameter	$\tau_0$	$G_d$ (J/m <sup>2</sup> )	$\beta$
Taking values	1.31	1.08	0.308

where  $\tau_0$  is the initial sliding-friction force,  $G_d$  is the chemical-debonding energy and  $\beta$  is the friction factor.

#### **Fiber-Matrix Joint Constitutive-relation Model**

As shown in Fig. 3, to realistically simulate the complete mechanical behavior of fibers in the matrix,

this paper considers the elastic stage in addition to the debond stage and slip stage in Li's theory. Based on drawing the load-displacement curve of monofilament, a fiber-matrix joint constitutive-relation model is proposed. The material properties as plant fibers are endowed with fiber units to reflect the interfacial interaction between plant fibers and cement matrix.

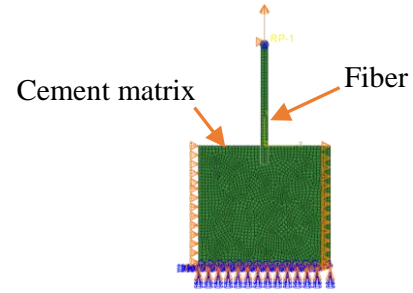


**Figure (3): Single-fiber pull-out simulation diagram**

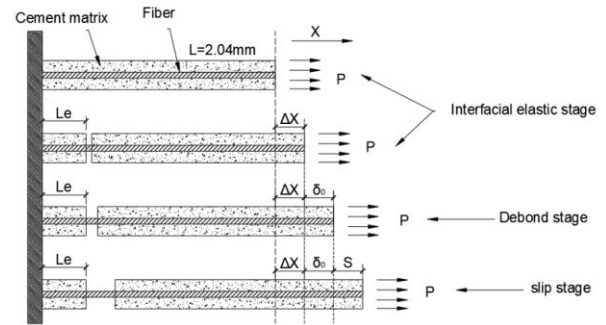


**Figure (4): Fiber-matrix joint constitutive-relation model analysis unit**

As shown in Fig. 4, since the plant fiber is embedded in the cement matrix and will not slip relative to the matrix, it is necessary to take the displacement  $x$  on the right surface of the cement matrix in Fig. 4 as the elongation length of the fiber in the matrix, which is called the nominal elongation distance of the fiber and  $p$  is the actual load on the fiber. In the three stages, because the deformation of the mortar matrix is very small, it can be ignored in the analysis process. The relative displacement  $x$  generated by the complex after the matrix cracking in the elastic stage is mainly due to the elastic deformation of the interface between the fiber and the matrix at the crack. So, the interfacial elasticity phase displacement on the surface of the substrate right  $\Delta x$  can be obtained by Eq. (5):

$$\Delta x = \frac{4P_d L_f}{\pi E_f d_f^2} \quad (5)$$

where  $P_{d0}$  is the initial load value of the fiber at the debonding stage,  $E_f$  is the elastic modulus of the fiber,  $L_f$  is the fiber length and  $d_f$  is the fiber diameter.

When  $P$  reaches the initial load  $P_{d0}$  in the debonding stage, the plant fiber begins to debond from the cement matrix and the embedment depth  $L_e$  of the fiber is determined by the cracking position of the fiber. Debonding in the fiber phase, the fiber elongation  $\Delta x$  relative sliding displacement is very small and is therefore negligible and the debonding-phase displacement is still chosen  $\delta_0$  of the theory of Li. The slip stage of fibers is consistent with the hypothesis in Li's theory. The fiber is considered to be a rigid body and only the rigid-body translational displacement  $S$  of the fiber is considered.

Because the fiber burial depth is also an important factor affecting the load-displacement curve of a single-fiber pull-out, the load-displacement curves of fibers with different burial depths are also different. From Eq. (2), it can be seen that the fiber burial depth mainly affects the pull-out distance  $\delta_0$  of the complete debonding of the fiber and has no effect on the changing trend of the debonding stage of the fiber and the fiber burial depth has a significant effect on the slip phase. Therefore, a two-dimensional single-fiber pull-out simulation is carried out for fibers with different burial depths.

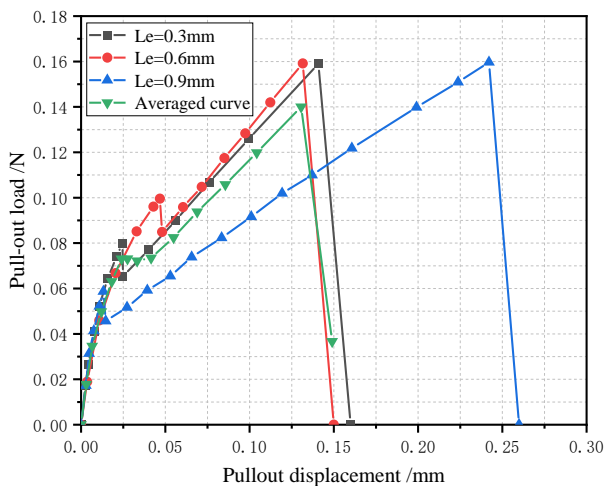


**Figure (5): Load-displacement curves of fiber monofilaments with different burial depths**

From Fig. 5, it can be seen that the bond-slip constitutive of plant fiber with 0.6mm burial depth is

closer to the average constitutive. Therefore, this paper uses the fiber-matrix joint constitutive-relation model with 0.6mm burial depth, as shown in Fig. 6.

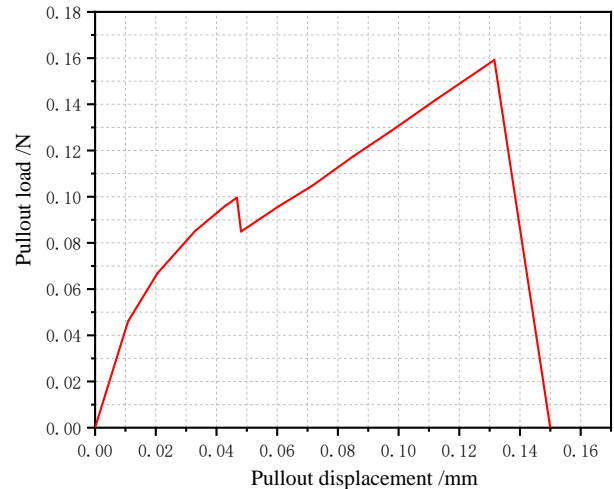


**Figure (6): Fiber-matrix joint constitutive load-displacement curve**

In finite-element software, stress and strain values are required when the fiber-matrix joint constitutive-relation model is input. In this regard, the ordinate is divided by the fiber cross-sectional area and the abscissa is divided by the fiber length to obtain stress and strain, respectively. The resulting fiber-matrix joint constitutive-relation model is shown in Fig. 7.

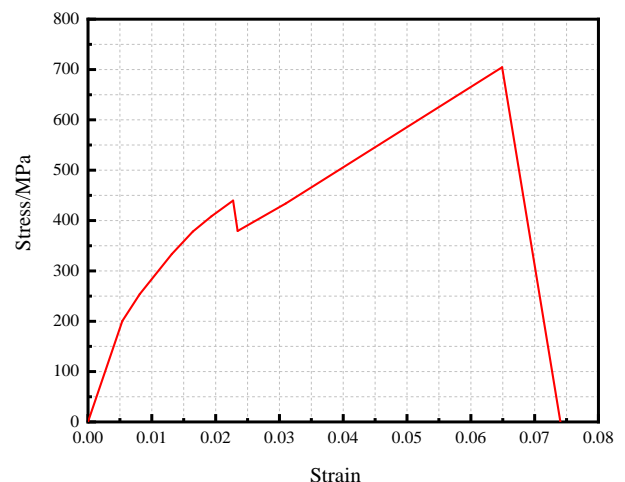


**Figure (7): Fiber-matrix joint constitutive stress-strain curve**

## NUMERICAL SIMULATION OF AXIAL TENSILE

### *Element Type and Mesh Size*

The refined FE models of the specimens were developed by ABAQUS/Explicit. The solid elements (C3D8R) were adopted for cement, whilst truss elements (T3D2) were employed for the plant fiber.

Different mesh sizes were utilized to strike a balance between accuracy and consumed time. The two ends of the tensile specimen are 3mm grids to improve calculating efficiency. For areas where the fracture or large deformation may occur (the middle cement matrix and fiber part of the specimen), a refined mesh size of 1 mm was used to ensure the simulation accuracy.

### *Boundary Conditions*

With the coupling command, the left end of the PFRCC panel is coupled to the reference point using the coupling manner, binding all degrees of freedom of the reference point except for the degrees of freedom in the X direction. The finite-element model is loaded by displacement and a displacement along X is applied to the reference point. The boundary conditions of the reference point are  $U_1 = 0.8$ ,  $U_2 = U_3 = 0$  and  $UR_1 = UR_2 = UR_3 = 0$ . The right end of the PFRCC panel is completely fixed and the boundary conditions are  $U_1 = U_2 = U_3 = 0$  and  $UR_1 = UR_2 = UR_3 = 0$ . The fiber is embedded in the entire model. The uniaxial tensile numerical simulation is consistent with the test and it is rounded to prevent stress concentration, as shown in Fig. 8. The research methodology of tensile properties of the PFRCC panel is shown in Fig. 9.

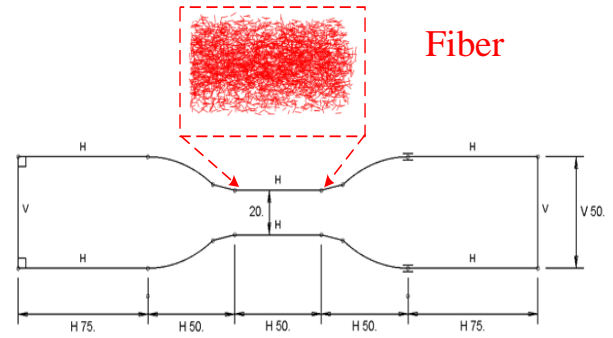


**Figure (8): PFRCC panel uniaxial tensile simulation specimen diagram**

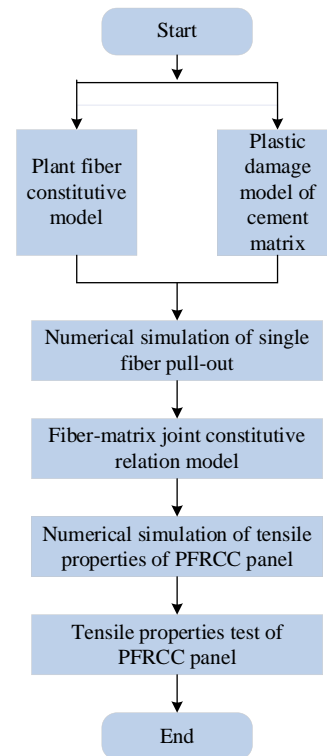


**Figure (9): Flowchart of research methodology for tensile properties of PFRCC panel**

Stress Nephogram

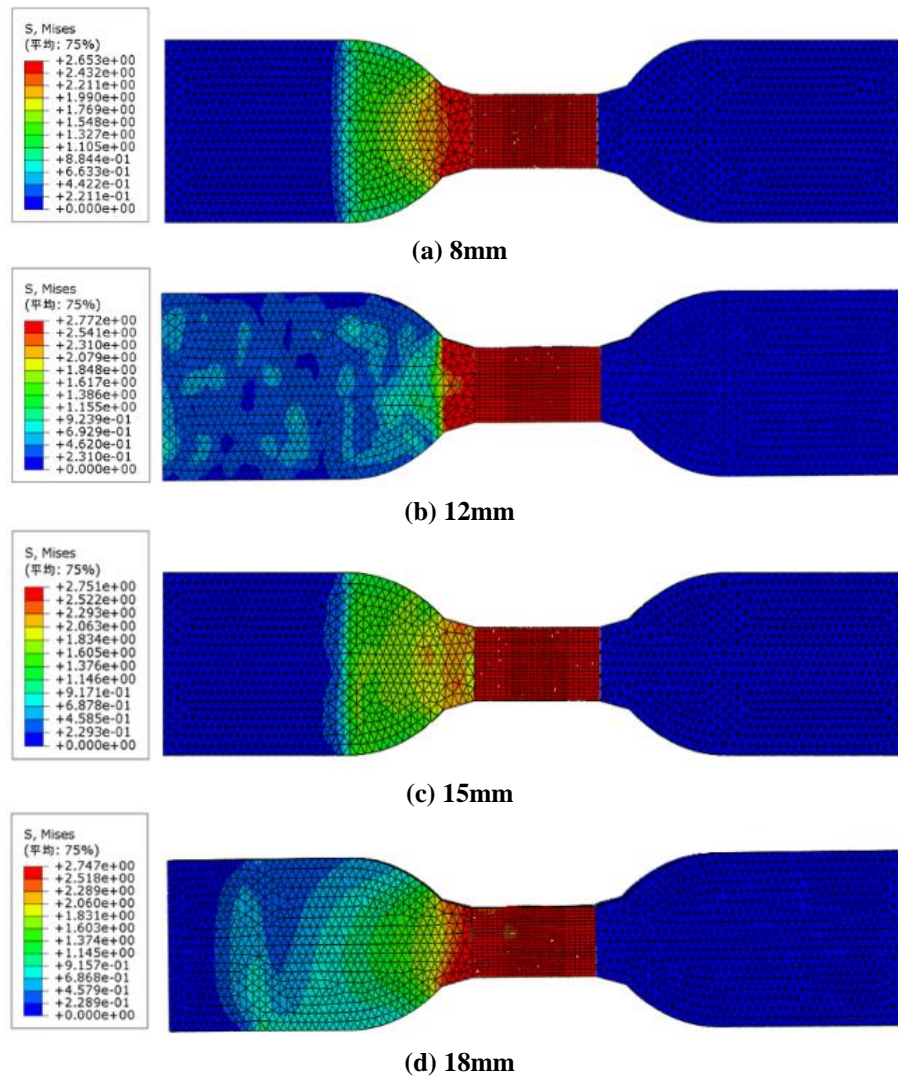


Figure (10): Uniaxial tensile-stress nephogram of PFRCC panel

It can be seen from Fig. 10 that the stress-distribution pattern of dumbbell-type PFRCC panel specimen in the uniaxial tension direction is as follows: as the section width decreases, the stress increases. According to the mechanics of materials, the numerical results of stress are in accordance with the theoretical law. The damage form of finite-element simulation also conforms to the damage law of the test and the middle part of the dumbbell-type specimen breaks, so proving the correctness of finite-element simulation. The tensile-

strength of the specimen is calculated by Eq. (6) and the calculation results are shown in Table 3.

$$\sigma_1 = \frac{F_{\max}}{b \times t} \tag{6}$$

where  $\sigma_1$  is tensile-strength (MPa),  $F_{\max}$  is the maximum load when the specimen is damaged (N),  $b$  is the average tensile section width of the specimen (mm) and  $t$  is the average length of the shear plane of a tensile section thickness of the specimen (mm).

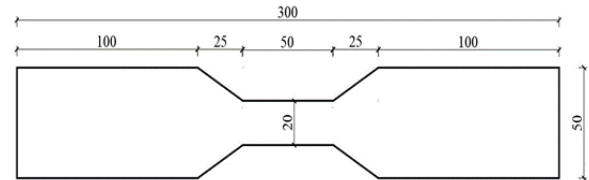
**Table 3. Simulation results of uniaxial tensile-strength of PFRCC panel**

Specimen number	b×t (mm)	F <sub>max</sub> (N)	Tensile strength (MPa)
A	20×8	424.0	2.65
B	20×12	664.8	2.77
C	20×15	825.0	2.75
D	20×18	986.4	2.74

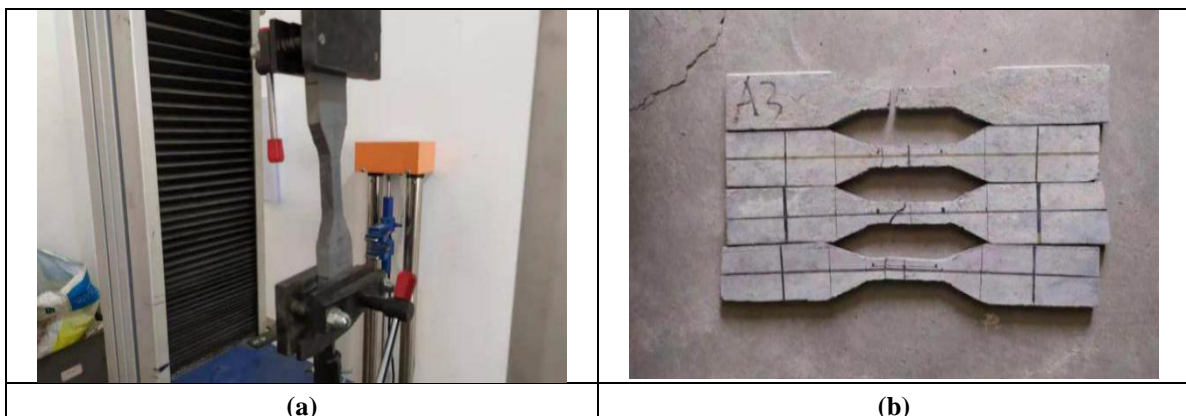
**Test verification**

This test is to verify the correctness of the numerical simulation of the axial tensile mechanical properties of PFRCC materials. The PFRCC panel is designed as the dumbbell-shaped specimen, as shown in Fig. 11. The test data was recorded independently by the universal mechanical-testing machine test system. The PFRCC material was prepared in accordance with the numerical simulation. As shown in Table 4, the cement matrix of plant fiber-reinforced cementitious composites' panels was composed of ordinary 42.5 Portland cement, fly ash, quartz sand, water and polycarboxylate superplasticizer. The standard cube c samples with a size of 150mm×150mm×150mm were prepared and the 28-day compressive strength of the cement matrix is 45.8 MPa. The plant fiber used in plant fiber-reinforced cementitious composites' panels was bamboo-pulp fiber

with an average length of about 2.04 mm and its volume fraction was about 6 %. The bamboo-pulp fiber was treated with 2% NaOH solution at room temperature for 60 minutes and then washed with water. Finally, it was dried at 100°C. The rate of loading is 10mm/min and was continuously loaded until the specimen was destroyed, as shown in Fig. 12. The test results are shown in Table 5.

**Figure (11): Processing size of PFRCC panel axial tensile specimen****Table 4. Composition of the cement matrix**

42.5 Cement (kg/m <sup>3</sup> )	Fly ash (kg/m <sup>3</sup> )	Quartz sand (kg/m <sup>3</sup> )	Water (kg/m <sup>3</sup> )	Superplasticizer (kg/m <sup>3</sup> )	Water-binder ratio (W/B)
550	650	550	395	5.225	0.33

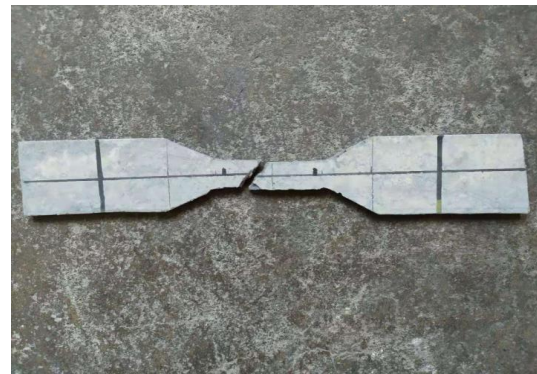
**Figure (12): PFRCC panel axial tensile test diagram**

**Table 5. Axial tensile-strength test results of PFRCC panels**

Specimen number	b×t (mm)	F <sub>max</sub> (N)	Tensile-strength (MPa)
I	20×8	404.24	2.53
II	20×12	616.75	2.56
III	20×15	768.25	2.56
IV	20×18	866.99	2.41



**(a) Specimen failure mode 1**



**(b) Specimen failure mode 2**

**Figure (13): Failure modes of axial tensile test**

As shown in Fig. 13, there are two main failure modes in the axial tensile test of the PFRCC panel. Failure mode 1 breaks at the variable cross-section and stress concentration occurs, indicating that the uneven processing of the specimen produces eccentric tension. Failure mode 2 breaks in the middle of the equal straight section, indicating that the specimen is more uniform

and achieves axial tension. It can be seen that the defects of the specimen should be avoided as much as possible in the process of making the specimen. During the axial tensile test of the PFRCC panel, the main crack in the middle of the specimen is the effective failure mode of the specimen.

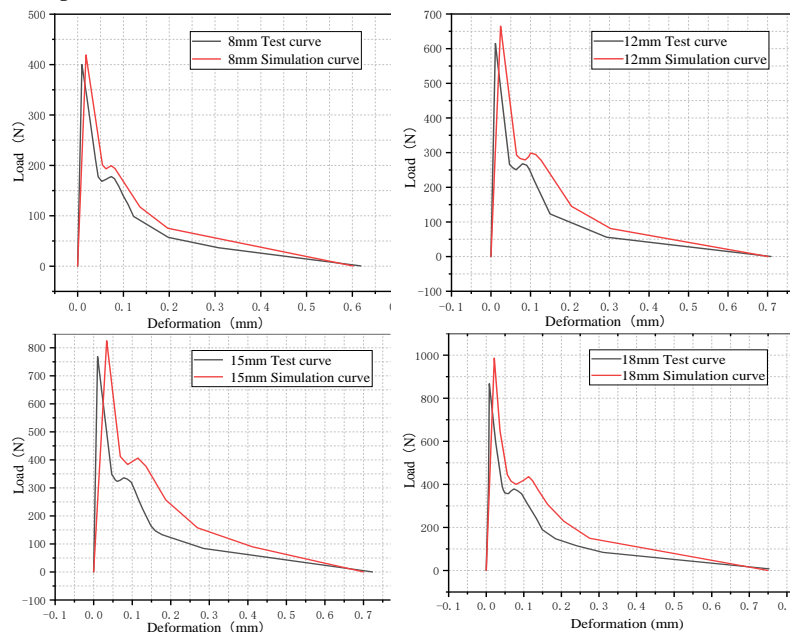


**Figure (14): Uniaxial tensile load-deformation simulation curve of PFRCC panel**

As shown in Fig. 14, the trend of the axial tensile load-deformation test curve and that of the simulation curve of the PFRCC panel are the same, which proves the correctness of the mechanical model of the PFRCC material proposed in this paper. According to the simulation results, the peak tensile-strength failure load of the 8mm PFRCC panel is 424.0N, its peak deformation is 0.018mm and its peak tensile strain is about 0.036%. The failure peak load of the 12mm PFRCC panel is 664.8N, its peak deformation is 0.024mm and its peak tensile strain is about 0.048%. The peak tensile-strength load of the 15mm PFRCC panel is 825.0N, its peak deformation is 0.033mm and its peak tensile strain is about 0.052%. The tensile-strength failure peak load of the 18mm PFRCC panel is 986.4N, its peak deformation is 0.021mm and its peak tensile strain is about 0.042%. The 28-day peak tensile strain of the cement matrix is about 0.015% and the peak tensile strain of a PFRCC panel with a plant-fiber content of about 6% is 2.93 times that of the cement matrix. From the load-deformation curve, it can be seen that the load in reaching the first-limit load peak and the bearing drops sharply to a certain value. At this time, the plant fiber bridged between the cracks plays a bearing role and the bearing capacity will rise in a small range, but the bearing capacity rises very little and then, the bearing capacity decreases to 0, resulting in failure and failure of the specimen.

From the above, it can be seen that the thickness of 8mm to 12mm is increased by 4mm and the  $F_{max}$  of failure load is increased by 56.7%. The thickness of 12mm to 15mm is increased by 3mm and the failure load is increased by 24.1%. The thickness of 15mm to 18mm is increased by 3mm and the failure load is increased by 19.5%. The average tensile strength of 8mm, 12mm, 15mm and 18mm PFRCC panels is 2.65MPa, 2.77MPa, 2.75MPa and 2.74MPa. The tensile strength of PFRCC panels does not change much with the increase in the thickness of PFRCC panels. The results show that the tensile strength of the PFRCC panel is not related to its thickness and the tensile strength of the PFRCC panel is about 2.73MPa.

As shown in Fig. 14, the tensile curves of PFRCC panels with different thicknesses are compared and the data is analyzed. It is shown that the failure load of PFRCC panels increases with the increase of thickness, while the peak deformation and peak tensile strain of

PFRCC panels do not change with the increase of thickness. The peak deformation of the PFRCC panels with 6% plant-fiber content is about 0.024mm and the peak tensile strain is about 0.044%, which is 2.93 times that of the cement matrix. Moreover, it can be found that the tensile-strength curve of the PFRCC panels can be divided into three stages: (1) Elastic stage: the curve basically shows a linear change. At this stage, the cement matrix and the fiber bear the load together and no cracks appear before reaching the peak load of the curve failure. (2) Yield stage: the first crack begins to appear in the specimen and the curve drops abruptly and then turns. Thereafter, the load-bearing capacity increases due to the fibers bridging between the cracks acting as load bearings. At the same time, the deformation also continues to increase. The number of fluctuations on the curve represents the number of cracks. (3) Failure stage: the matrix completely loses its loading-bearing capacity. In this stage, the material strain increases and the stress decreases; namely, the strain-softening phenomenon.

## CONCLUSIONS

In this paper, the refined FE models of the PFRCC panel are established by ABAQUS. The tensile properties of PFRCC panels with four thicknesses were analyzed based on the established FE model and the axial tensile test was used to verify it. The main conclusions drawn are as follows:

(1) For PFRCC panels with 8 mm, 12 mm, 15 mm and 18 mm thicknesses, the uniaxial tensile failure peak loads are 424.0 N, 664.8 N, 825 N and 986.4 N, respectively. The failure load  $F_{max}$  increases by 56.7%, 24.1% and 19.5% for a thickness from 8 mm to 12 mm (4 mm increase), 12 mm to 15 mm (3 mm increase) and 15 mm to 18 mm (3 mm increase), respectively.

(2) The PFRCC panel has a peak tensile deformation of about 0.014 mm, a peak tensile strain of about 0.044%, 2.93 times that of the cement matrix and a tensile-strength of about 2.73 MPa, proving that adding plant fiber can increase the concrete toughness and increasing PFRCC panel thickness can improve its tensile capacity, but not affecting its tensile strength. The tensile load-deformation curve of the PFRCC panel can be divided into elastic, yield and failure stages.

(3) This paper proposed a finite-element modeling

method for fiber-reinforced cementitious composites. Using the fiber-matrix joint constitutive-relation model instead of the constitutive model of fiber can better reflect the mechanical properties of fiber in the cement matrix. The trend of the axial tensile load-deformation test curve and that of the simulation curve of the PFRCC panel are the same, which proves the correctness of the mechanical model of the PFRCC material proposed in this paper.

### Conflict of Interests

The authors declare that there is no conflict of

interests regarding the publication of this paper.

### Data-availability Statement

Model parameters, as well as model calculation results that support the findings of this study, are available from the corresponding author upon reasonable request.

### Acknowledgments

This research is supported in part by the National Natural Science Foundation of China (Grant number: 51968045).

## REFERENCES

- Alrekabi, S., Cundy, A.B., Lampropoulos, A., Whitby, R.L.D., and Savina, I. (2017). "Mechanical performance of novel cement-based composites prepared with nano-fibres and hybrid nano-and micro-fibres". *Composite Structures*, 178, 145-156. <https://doi.org/10.1016/j.compstruct.2017.06.045>
- Bahja, B., Elouafi, A., Tizliouine, A., and Omari, L.H. (2021). "Morphological and structural analysis of treated sisal fibers and their impact on mechanical properties in cementitious composites". *Journal of Building Engineering*, 34, 102025. <https://doi.org/10.1016/j.job.2020.102025>
- Bi, J.H., Huo, L.Y., Zhao, Y., and Wang, Z.Y. (2021). "Constitutive model and mechanical properties of steel fiber-reinforced concrete". *Journal of Hunan University (Natural Sciences)*, 48 (07), 9-18.
- Chai Q.L. (2019). "Experimental study on material performance of engineered cementitious composite and numerical simulation of cantilever bending column". Lanzhou University of Technology.
- Ferreira, S.R., de Andrade Silva, F., Lima, P.R.L., and Toledo Filho, R.D. (2017). "Effect of hornification on the structure, tensile behavior and fiber-matrix bond of sisal, jute and curauá fiber cement-based composite systems". *Construction and Building Materials*, 139, 551-561. <https://doi.org/10.1016/j.conbuildmat.2016.10.004>
- Guo, Y.H., Li, L., Yang, C.X., and Shi, Y.Q. (2022). "Research progress of plant fiber-reinforced concrete". *Bulletin of the Chinese Ceramic Society*, 41 (10), 3347-3358.
- Kavya, B.R., Sureshchandra, H.S., Prashantha, S.J., and Shrikanth, A.S. (2022). "Prediction of mechanical properties of steel fiber-reinforced concrete using CNN". *Jordan Journal of Civil Engineering*, 16 (2).
- Kochova, K., Gauvin, F., Schollbach, K., and Brouwers, H.J.H. (2020). "Using alternative waste coir fibres as a reinforcement in cement-fibre composites". *Construction and Building Materials*, 231, 117121. <https://doi.org/10.1016/j.conbuildmat.2019.117121>
- Li, V.C. (1993). "From micromechanics to structural engineering: The design of cementitious composites for civil-engineering applications". *Doboku Gakkai Ronbunshu*, 1993 (471), 1-12. [https://doi.org/10.2208/jscej.1993.471\\_1](https://doi.org/10.2208/jscej.1993.471_1)
- Li, V.C., Banthia, N., Bentur, A., and Mufti, A. (1998). "Engineered cementitious composites: Tailored composites through micromechanical modeling to appear in fiber-reinforced concrete". Present and the Future, Canadian Society of Civil Engineers.
- Li, S., Hu, B., and Zhang, F. (2018). "Preparation and properties of glass fiber/plant fiber-reinforced cementitious composites". *Science of Advanced Materials*, 10 (7), 1028-1035. <https://doi.org/10.1166/sam.2018.3288>
- Liu, W.H., and Zhang, L.W. (2019). "A novel XFEM cohesive fracture framework for modeling nonlocal slip in randomly discrete fiber-reinforced cementitious composites". *Computer Methods in Applied Mechanics and Engineering*, 355, 1026-1061. <https://doi.org/10.1016/j.cma.2019.04.040>

- Mathews, M.E., Anand, N., Kodur, V.K., and Arulraj, P. (2021). "The bond strength of self-compacting concrete exposed to elevated temperature". *Proceedings of the Institution of Civil Engineers-Structures and Buildings*, 174 (9), 804-821. <https://doi.org/10.1680/jstbu.20.00105>
- Santos, R.F., Ribeiro, J.C.L., de Carvalho, J.M.F., Magalhães, W.L.E., Pedroti, L.G., Nalon, G.H., and de Lima, G.E.S. (2021). "Nanofibrillated cellulose and its applications in cement-based composites: A review". *Construction and Building Materials*, 288, 123122. <https://doi.org/10.1016/j.conbuildmat.2021.123122>
- Shang, J., Zhao, T.J., Wang L.Q., Guo S.Y., and Wang, P.G. (2019). "Research on direct tensile experiments of high-ductile vegetable fiber-reinforced cementitious composites". *Bulletin of the Chinese Ceramic Society*, 38 (01), 218-223+230.
- Wang, X., Zhai, D.D., Guo, Y.C., Wang, Z., Zhao, T., and Liu, J. (2017). "Mechanical property of sisal fiber enhancing concrete". *Bulletin of the Chinese Ceramic Society*, 36 (07), 2488-2491.
- Yao, Q.Y., Lu, C.Y., Luo, Y.J., Xie, Z.Z., and Teng, X.D. (2022). "Tensile properties and constitutive model of PE/PVA fiber sea-sand ECC". *Journal of Building Materials*, 25 (09), 976-983.
- Zukowski, B., de Andrade Silva, F., and Toledo Filho, R.D. (2018). "Design of strain-hardening cement-based composites with alkali-treated natural curauá fiber". *Cement and Concrete Composites*, 89, 150-159. <https://doi.org/10.1016/j.cemconcomp.2018.03.006>